

Early Science with the Large Millimeter Telescope: Observations of dust continuum and CO emission lines of cluster-lensed submillimetre galaxies at $z = 2.0 - 4.7$

J. A. Zavala^{*1}, M. S. Yun², I. Aretxaga¹, D. H. Hughes¹, G. W. Wilson², J. E. Geach³, E. Egami⁴, M. A. Gurwell⁵, D. J. Wilner⁵, Ian Smail⁶, A. W. Blain⁷, S. C. Chapman⁸, K. E. K. Coppin³, M. Dessauges-Zavadsky⁹, A. C. Edge¹⁰, A. Montaña^{11,1}, K. Nakajima⁹, T. D. Rawle¹², D. Sánchez-Argüelles¹, A. M. Swinbank¹⁰, T. M. A. Webb¹³, M. Zeballos¹

¹Instituto Nacional de Astrofísica, Óptica y Electrónica (INAOE), Luis Enrique Erro 1, Sta. Ma. Tonantzintla, Puebla, Mexico

²Department of Astronomy, University of Massachusetts, Amherst, MA 01003, USA

³Center for Astrophysics Research, Science and Technology Research Institute, University of Hertfordshire, Hatfield, AL10 9AB, UK

⁴Steward Observatory, University of Arizona, 933 North Cherry Avenue, Tucson, AZ 85721, USA

⁵Harvard-Smithsonian Center for Astrophysics, 60 Garden street, Cambridge, MA 02478, USA

⁶Centre for Extragalactic Astronomy, Department of Physics, Durham University, South Road, Durham DH1 3LE, UK

⁷Department of Physics and Astronomy, University of Leicester, University Road, Leicester LE1 7RH, UK

⁸Department of Physics and Atmospheric Science, Dalhousie University, 6310 Coburg Rd., Halifax, NS B3H 4R2, Canada

⁹Observatoire de Genève, Université de Genève, 51 Ch. des Maillettes, 1290 Versoix, Switzerland

¹⁰Institute for Computational Cosmology, Department of Physics, Durham University, South Road, Durham DH1 3LE

¹¹Consejo Nacional de Ciencia y Tecnología (CONACyT), Av. Insurgentes Sur 1582, 03940, D.F., Mexico

¹²ESAC, ESA, PO Box 78, Villanueva de la Canada, E-28691 Madrid, Spain

¹³Department of Physics, Ernest Rutherford Building, 3600 rue University, McGill University, Montreal, QC H3A 2T8, Canada

Accepted 2015 June 15. Received 2015 June 15; in original form 2014 December 23

ABSTRACT

We present Early Science observations with the Large Millimeter Telescope, AzTEC 1.1 mm continuum images and wide bandwidth spectra (73 – 111 GHz) acquired with the Redshift Search Receiver, towards four bright lensed submillimetre galaxies identified through the *Herschel* Lensing Survey-snapshot and the Submillimetre Common-User Bolometer Array-2 Cluster Snapshot Survey. This pilot project studies the star formation history and the physical properties of the molecular gas and dust content of the highest redshift galaxies identified through the benefits of gravitational magnification. We robustly detect dust continuum emission for the full sample and CO emission lines for three of the targets. We find that one source shows spectroscopic multiplicity and is a blend of three galaxies at different redshifts ($z = 2.040, 3.252$ and 4.680), reminiscent of previous high-resolution imaging follow-up of unlensed submillimetre galaxies, but with a completely different search method, that confirm recent theoretical predictions of physically unassociated blended galaxies. Identifying the detected lines as ^{12}CO ($J_{up} = 2 - 5$) we derive spectroscopic redshifts, molecular gas masses, and dust masses from the continuum emission. The mean H_2 gas mass of the full sample is $(2.0 \pm 0.2) \times 10^{11} M_{\odot}/\mu$, and the mean dust mass is $(2.0 \pm 0.2) \times 10^9 M_{\odot}/\mu$, where $\mu \approx 2 - 5$ is the expected lens amplification. Using these independent estimations we infer a gas-to-dust ratio of $\delta_{\text{GDR}} \approx 55 - 75$, in agreement with other measurements of submillimetre galaxies. Our magnified high-luminosity galaxies fall on the same locus as other high-redshift submillimetre galaxies, extending the $L'_{\text{CO}}\text{-}L_{\text{FIR}}$ correlation observed for local luminous and ultraluminous infrared galaxies to higher far-infrared and CO luminosities.

Key words: submillimetre: galaxies - galaxies: high redshift - galaxies: evolution - galaxies: ISM - cosmology: observations

1 INTRODUCTION

Observations of nearby galaxies with the *Infrared Astronomical Satellite* (IRAS) and the *Spitzer Space Telescope* (SST) have shown that a significant fraction of the far-infrared (FIR) emission is from galaxies at high redshift.

* E-mail: zavala@inaoep.mx

(FIR)/submillimetre background with the *Cosmic Background Explorer* (COBE), showed that the Universe emits a comparable energy density at infrared (IR) and submillimetre wavelengths as it does at optical and ultraviolet wavebands (e.g. Soifer et al. 1987; Puget et al. 1996; Fixsen et al. 1998). A breakthrough in resolving this background came with the discovery of a large population of bright sources at high redshift through single-dish telescopes observations at submillimetre wavelengths (e.g. Smail et al. 1997; Barger et al. 1998; Hughes et al. 1998). These (sub)millimetre-selected galaxies (hereafter SMGs) are characterized by large FIR luminosities ($\gtrsim 10^{12} L_{\odot}$), large star formation rates (SFRs, $\gtrsim 300 M_{\odot} \text{ yr}^{-1}$), large gas reservoirs ($\gtrsim 10^{10} M_{\odot}$), and a number density that is high compared to local ultra-luminous IR galaxies (Chapman et al. 2005; see also review by Casey et al. 2014).

However, identifying and understanding the nature of these sources has proven to be challenging due to the low angular resolution of single-dish telescopes and the faintness of these galaxies in the rest-frame optical and ultraviolet bands, which makes the association with the correct counterpart difficult (Blain et al. 2002). High-resolution radio/mid-infrared observations have often been used to identify counterpart galaxies on 1 – 2 arcsec scales (e.g. Ivison et al. 2002; Pope et al. 2008), providing the precision needed to target optical redshifts, which are essential to understand the physical nature of these sources. However, recent submillimetre interferometric observations have shown that resourcing to surrogate wavelengths could miss ~ 45 per cent of SMGs, and of those which are claimed to be identified, approximately one third are incorrect (Smolčić et al. 2012; Hodge et al. 2013; Simpson et al. 2015). Furthermore, the use of these wavelengths suffers from a well-known systematic bias against high-redshift ($z \gtrsim 3$) sources and therefore our understanding of these galaxies could be incomplete.

Millimetric spectroscopy provides the best way to determine redshifts for this population of galaxies, since they are expected to have luminous emission lines in the millimetre bands. Furthermore, the cold molecular phase of the interstellar medium (ISM) is an excellent tracer of the molecular gas reservoir, and the overall galaxy dynamics. For instance, CO(1–0) has been extensively used to map the molecular gas content of this kind of galaxies (e.g. Carilli et al. 2010; Harris et al. 2010; Ivison et al. 2010; Riechers et al. 2011; Bothwell et al. 2013; see also review by Carilli & Walter 2013). When combined with the SFRs (or FIR luminosities), gas masses also provide estimations of the star formation efficiencies (SFE), which is an important parameter for models of galaxy evolution (e.g. Santini et al. 2014; Dessauges-Zavadsky et al. 2015).

However, CO spectroscopy is very time consuming, when re-tuning receivers to search for molecular line emission, requiring entire nights to detect a single source, and in some cases with no successful detection (e.g. Greve et al. 2005; Huynh et al. 2014). This method has only recently become competitive with the increased bandwidth of (sub)mm facilities, but is still not yet sufficiently efficient to obtain redshifts for substantially large samples of unlensed SMGs (Bothwell et al. 2013). On the other hand, CO line observations for strongly lensed systems can be obtained more easily, representing one route to study the molecular gas content of SMGs (e.g. Knudsen et al. 2009; Cox et al. 2011; Harris et al. 2012; Weiß et al. 2013). Although in some cases, differential magnification could affect the properties derived from observations (e.g. line ratios, Serjeant 2012), cluster lensing provide us more reliable results since is rare to find this kind of magnification gradients.

Here we present new observations of a sample of four cluster-

lensed SMGs, discovered by the *Herschel* Lensing Survey-snapshot (HLS-snapshot, Egami et al. in preparation; see also Egami et al. 2010) and subsequently detected with the Submillimetre Common-User Bolometer Array-2 (SCUBA-2, Holland et al. 2013) on the James Clerk Maxwell Telescope (JCMT) as part of the SCUBA-2 Cluster Snapshot Survey (S2CSS, Geach et al. in preparation). The new observations comprise imaging from the 1.1 mm continuum camera AzTEC (Wilson et al. 2008) and the wide bandwidth (73 – 111 GHz) spectrometer Redshift Search Receiver (RSR, Erickson et al. 2007) installed on the Large Millimeter Telescope *Alfonso Serrano* (LMT¹, Hughes et al. 2010), located on the summit of Volcán Sierra Negra (Tliltépetl), Mexico, at an altitude of ~ 4600 m. Combining the high sensitivity and bandwidth of the LMT instruments with the higher flux density of amplified galaxies, the detection of CO molecular lines and dust continuum can be reached in reasonable times, allowing us to derive spectroscopic redshifts, and therefore to inquire into the dust and gas properties in these galaxies.

In §2, we describe the sample selection, observations and data reduction. In §3, we describe the line identification, redshift estimations, and gas and dust properties. In §4, we discuss the implication of these results for the gas-to-dust ratio and SFE. Our results are summarized in §5.

All calculations assume a Λ cold dark matter cosmology with $\Omega_{\Lambda} = 0.68$, $\Omega_m = 0.32$, and $H_0 = 67 \text{ kms}^{-1} \text{ Mpc}^{-1}$ (Planck Collaboration et al. 2013).

2 OBSERVATIONS AND DATA REDUCTION

2.1 Sample selection and SCUBA-2/JCMT data

The four bright SMGs targeted here were originally discovered by the HLS-snapshot survey, which has obtained shallow but nearly confusion-limited Spectral and Photometric Imaging Receiver (SPIRE) images of 279 Massive Cluster Survey (MACS) clusters. Three of the four galaxies have a SPIRE flux densities of more than 100 mJy at either 250, 350 or 500 μm , and have subsequently produced bright detections in the S2CSS. The remaining target (HLS J102225.9+500536) was detected by HLS below the 100 mJy threshold but was comparably bright at 850 μm . The analysis of the *Herschel* data and their optical-IR counterparts will be presented elsewhere by the HLS team.

S2CSS exploited poor weather conditions at the JCMT (opacities of $\tau_{225\text{GHz}} = 0.12\text{--}0.2$) to search for bright ($S_{850\mu\text{m}} > 30$ mJy) gravitationally lensed SMGs, comparable to the ‘Cosmic Eyelash’ (Swinbank et al. 2010), in the cores of hundreds of rich clusters of galaxies, primarily selected from the MACS and SMACS surveys (e.g. Ebeling et al. 2001; see also target selection of the HLS in Egami et al. 2010). The ‘Cosmic Eyelash’ is a typical SMG at $z \approx 2.3$ with an intrinsic flux of $S_{870} \sim 3$ mJy, which is magnified 30 times by a foreground cluster, appearing as an $S_{870} \sim 106$ mJy source. The high magnification and spatially-resolved structure allows a very detailed study of the internal structure and chemistry of this galaxy on < 100 pc scales. Although rare, the bright nature of these sources makes them detectable at high significance even when observing conditions are relatively poor. For each cluster target a 30 minute DAISY scan map was obtained with SCUBA-2, which allowed the detection of luminous SMGs within a few

¹ www.lmtgtm.org

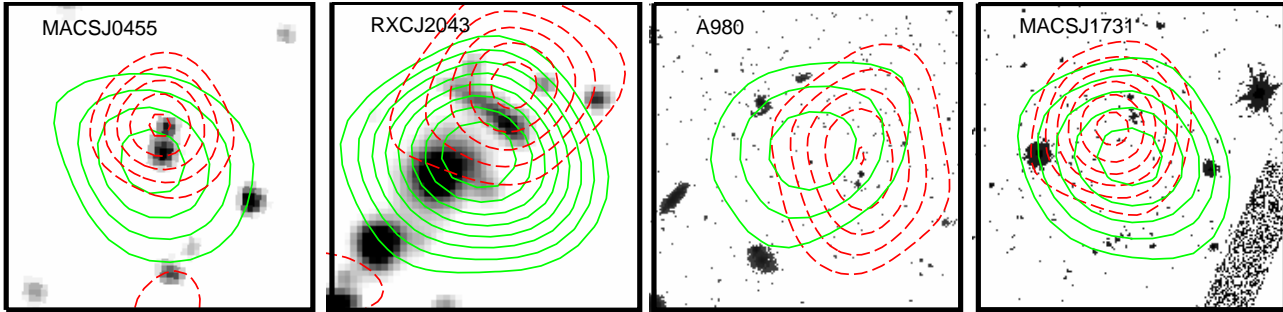


Figure 1. From left to right, 30×30 arcsec² Infrared Array Camera (IRAC)/*Spitzer* images in the $3.6 \mu\text{m}$ band at the SCUBA-2 position of HLS J045518.0+070103 and HLS J204314.2–214439 and *HST* images in the $F606W$ band at the position of HLS J102225.9+500536 and HLS J173140.8+225040. The SCUBA-2 $850 \mu\text{m}$ and AzTEC 1.1mm S/N contours are also shown in green (solid line) and red (dashed line), respectively. Contour levels start at 1.5σ and are spaced in steps of 1.5σ . See the electronic edition of the journal for a colour version of this figure.

Table 1. LMT observing log for data taken during the Early Science Phase in 2014. Column 1, name of the targeted galaxies; columns 2, 3, and 4: dates, opacities and integration times of AzTEC observations; columns 5, 6, and 7: dates, opacities and integration times of RSR observations.

ID	Date	AzTEC		Date	RSR	
		Opacities ($\tau_{225\text{GHz}}$)	t_{int} (min)		Opacities ($\tau_{225\text{GHz}}$)	t_{int} (min)
HLS J045518.0+070103	Feb 10	0.12	20	Feb 19, Mar 02, Apr 02	0.06, 0.17, 0.26–0.29	45, 45, 20
HLS J102225.9+500536	Jan 31	0.10	20	Mar 27, 29, Apr 02, 07	0.17, 0.15, 0.20, 0.15	10, 60, 50, 35
HLS J173140.8+225040	Mar 21, May 18	0.12, 0.18	4, 10	Apr 21, May 03	0.30, 0.30	30, 75
HLS J204314.2–214439	May 14, 16	0.20, 0.22	10, 10	May 08, 12, 18, 25, 26	0.46–0.57, 0.29–0.32, 0.13–0.15, 0.42–0.44, 0.35	90, 30, 50, 60, 30

arc minutes from the cluster cores (depending on source brightness). The data were reduced with the Sub-Millimetre User Reduction Facility (SMURF; Chapin et al. 2013), following a procedure described in Geach et al. (2013) where the map making was optimized for point-source detection. Typical root mean squared noise (rms) noise in individual $850\text{-}\mu\text{m}$ maps was 5–10 mJy (see Table 2).

We conducted observations with AzTEC and RSR on the LMT towards a sample of four $850 \mu\text{m}$ sources that represent some of the most secure ($> 5\sigma$) detections within S2CSS around the clusters MACS J0455.2+0657, Abell 980 (MACS J1022.4+5006), MACS J1731.6+2252, and RXCJ2043.2–2144 (MACS J2043.2–2144) at $z = 0.425, 0.158, 0.366$, and 0.204 , respectively (Ebeling et al. 1998, 2010; Böhringer et al. 2004; Mann & Ebeling 2012). Postage stamps of *Spitzer* or *Hubble Space Telescope* (*HST*) images, and overlaid with SCUBA-2 and AzTEC contours at these positions are shown in Fig. 1. Details of these bright galaxies, HLS J045518.0+070103, HLS J102225.9+500536, HLS J173140.8+225040, and HLS J204314.2–214439, and their fluxes are given in Table 2.

2.2 AzTEC/LMT

Observations were obtained using the 1.1 mm continuum camera AzTEC on the LMT between 2014 January and May (see Table 1). During this Early Science Phase operation, only the inner 32-m diameter section of the telescope surface is illuminated, leading to an effective beam size of ~ 8.5 arcsec, a factor of ~ 2 better than the SCUBA-2 $850 \mu\text{m}$ -beam. The scanning technique provided a Lissajous pattern covering a 1.5 arcmin diameter region with uniform noise in the map centred at the SCUBA-2 position. Observa-

tions were conducted over several observing nights with an opacity range of $\tau_{225\text{GHz}} = 0.07 - 0.18$ and a typical integration time of ~ 20 min per source, achieving an rms of 2–3 mJy (see Table 1) in the individual maps.

Each individual AzTEC observation is composed of a set of timestreams which store all the bolometer sky signals, the projected position of the array on the sky and the weather conditions. Calibration is performed using observations of the asteroids Ceres and Pallas. To generate the final maps from the raw data we use the AzTEC Standard Pipeline described in detail by Scott et al. (2008).

In Table 2 we summarize the 1.1 mm photometry measurements from the AzTEC maps shown in Fig. 2. The AzTEC positions, which, for these observations, have a typical uncertainty of ~ 2 arcsec, are consistent with the SCUBA-2 positions within the 95 per cent confidence intervals, except for the case of HLS J204314.2–214439. However, as discussed in §3.1.4, our RSR spectrum has revealed three sources in the beam for this target and, therefore, the estimated positional uncertainty could be underestimated.

2.3 Redshift Search Receiver/LMT

Observations with RSR were obtained between 2014 February and May. The RSR has 4 pixels arranged in a dual beam, dual polarization configuration. The four broad-band receivers cover instantaneously the frequency range $73 - 111 \text{ GHz}$ with a spectral resolution of 31 MHz ($\sim 100 \text{ km s}^{-1}$ at 93 GHz). The current 32-m telescope gives us an effective beam size of 20 arcsec at 110 GHz and 28 arcsec at 75 GHz .

Observations were obtained at the SCUBA-2 positions of the four galaxies listed in Table 2, over several observing nights with an

Table 2. Summary of SCUBA-2 and AzTEC photometry. Column 1: name of the targeted galaxies; columns 2, 3, 4, and 5: position, 95 per cent confidence interval for positional uncertainties following the description by Ivison et al. (2007) for single sources, signal-to-noise ratio, and 850 μm flux density for SCUBA-2 observations; columns 6, 7, 8, and 9: same information for 1.1 mm AzTEC observations.

ID	SCUBA-2 position (J2000)	$\Delta(\alpha, \delta)$ (arcsec)	S/N	$S_{850\mu\text{m}}$ (mJy)	AzTEC position (J2000)	$\Delta(\alpha, \delta)$ (arcsec)	S/N	$S_{1.1\text{mm}}$ (mJy)
HLS J045518.0+070103	04:55:18.1, +07:01:01	3.2	7.0	37 ± 5	04:55:18.1, +07:01:05	1.6	8.0	23 ± 3
HLS J102225.9+500536	10:22:26.6, +50:05:39	4.1	5.5	45 ± 8	10:22:26.2, +50:05:41	2.2	5.9	11 ± 2
HLS J173140.8+225040	17:31:40.5, +22:50:35	2.6	8.5	49 ± 6	17:31:40.6, +22:50:37	1.3	9.8	25 ± 3
HLS J204314.2-214439	20:43:14.5, -21:44:37	1.7	13.0	66 ± 5	20:43:14.2, -21:44:43	1.5	8.4	29 ± 3

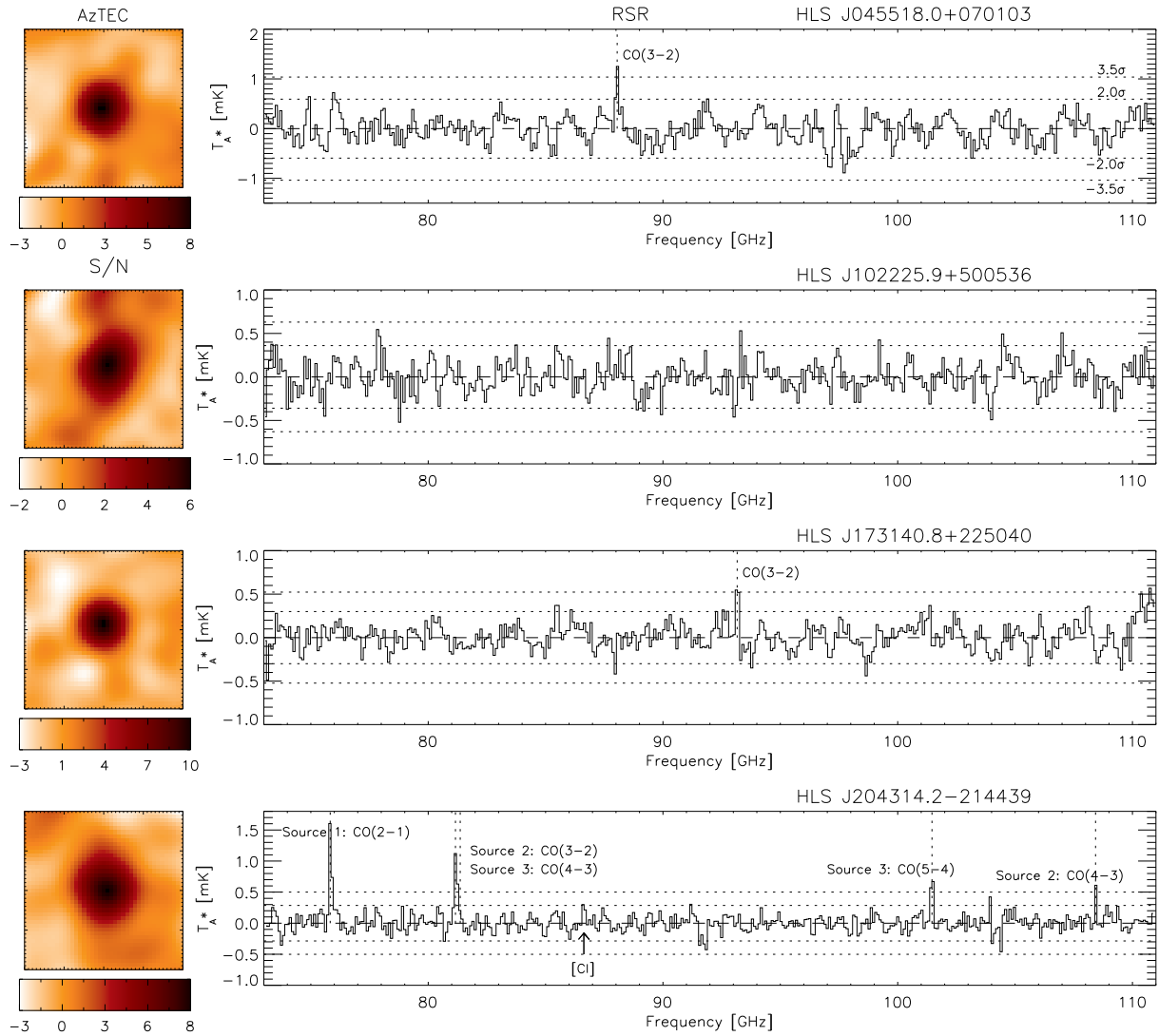


Figure 2. Left: 40×40 arcsec² AzTEC/LMT 1.1 mm S/N maps. All the maps are centred at the AzTEC positions listed in Table 2, and have been scaled for display purposes. Right: RSR/LMT spectra of the four HLS/S2CSS targets observed with the LMT. The RSR/LMT spectra have been rebinned into 3 pixels bins for better visualization. We mark with horizontal lines the 2 and 3.5 σ average noise level for each spectrum, where 1 σ has been calculated as the standard deviation of the whole binned spectrum after removing the identified lines. The transitions detected above the adopted threshold detection are marked with vertical dashed lines. In the spectrum of HLS J204314.2-214439 we have identified contributions from three different galaxies at different redshifts. We also mark with an arrow the expected position for the [CI] transition at $z = 4.680$ (see §3.1.4). See the electronic edition of the journal for a colour version of this figure.

opacity range of $\tau_{225\text{GHz}} = 0.13 - 0.57$ (see Table 1) and system temperatures of $T_{\text{sys}} = 90 - 140$ K with an average $T_{\text{sys}} \approx 100$ K. Pointing was performed every hour on bright millimetre sources, leading to a pointing accuracy (rms) ~ 2 arcsec.

The data were reduced and calibrated using Data REduction and Analysis Methods in PYthon (DREAMPY), which is the RSR data reduction pipeline software written by G. Narayanan. After flagging any data adversely affected by a hardware or software problem, a linear baseline is removed from each spectrum. The final spectra were obtained by averaging all scans using $1/\sigma^2$ weights. The spectra in antenna temperature units (T_A^*) are converted to flux density units using the conversion factors 6.4 and 7.6 Jy K^{-1} , for $73 < \nu \leq 92$ GHz and $92 < \nu < 111$ GHz, respectively, which are based on the calibration of Uranus and MWC349A, observed at $\text{EL} = 35^\circ - 75^\circ$, conducted in the Early Science Phase. Final spectra are shown in Fig. 2.

2.4 SMA observations

Observations on the cluster RXCJ2043.2–2144 were obtained with the Submillimeter Array (SMA) as a follow-up programme of the *Herschel* Lensing Survey (HLS) on 2012 May 8. After the LMT obtained a secure redshift for a $z = 4.68$ galaxy in this field (see §3.1.4), these data were reanalysed to search for the predicted [CII] line emission at $\nu = 334.6$ GHz as a means of further confirmation.

Observations were made using six antennas in a compact configuration. An on-source integration time of 3.9 h was obtained with the primary LO set to 342.046 GHz, using a single polarization SIS junction receiver with 4 GHz bandwidth per sideband. This bandwidth covered the expected frequency of the redshifted [CII] line for $z = 4.68$ (rest frequency 1900.54 GHz shifted to 334.60 GHz). The weather was very good, with the atmospheric opacity at 225 GHz varying from 0.05 to 0.07 throughout the observations. The synthesized beam size was $2.4 \times 1.9 \text{ arcsec}^2$. The primary flux density calibrator was Neptune, which provided a flux scale accurate to $\sim 5\%$. Instrumental and atmospheric gains were calibrated using complex gain calibrators J1924–292 (4.05 Jy), J2000–178 (0.46 Jy), and J2158–150 (1.66 Jy). The visibility data were resampled and averaged to a velocity resolution of 20 km s^{-1} , and then binned further to 100 km s^{-1} resolution in the imaging routine. The rms noise obtained in the final images was $15.2 \text{ mJy beam}^{-1}$ per 100 km s^{-1} channel.

These observations showed the presence of three distinct sources with a clear emission line feature at 334.6 GHz. Averaging consistent the spectra from these three positions produced the spectrum shown in Fig. 5 (rms of 8.8 mJy), which we identify as the [CII] transition. The analysis of the triple system and constraints to the lensing model of RXCJ2043.2–2144 (MACS J2043.2–2144) will be presented in a subsequent paper.

3 RESULTS

3.1 RSR analysis: line identification and spectroscopic redshifts

Since the main goal of these observations is to blindly search for molecular lines in our spectra, with no previous knowledge on the expected observed frequencies for these lines, it is important to define a criteria S/N threshold (ξ_{thresh}) that ensures the reliability of detections and that maintains the false detection rate very low.

To estimate the global noise of the spectra we fit the histogram

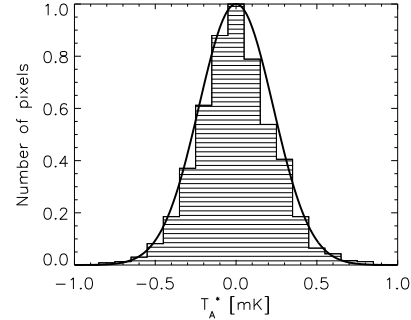


Figure 3. Histogram of pixel values in the RSR/LMT spectrum of HLS J102225.9+500536, as an example of the noise properties in the spectra. The histogram is well fitted by a Gaussian function, which is represented by the solid line. These Gaussian functions are used to make mock noise spectra in order to define a reliable threshold line detection.

of pixel values with Gaussian distributions. As can be seen in Fig. 3, a Gaussian fit reproduces very well the spectrum, and can be used as an estimation of the average noise. This is true for all the acquired spectra, achieving fits of $\chi^2_{\text{red}} = 0.57 - 0.96$. Using these Gaussian distributions, we make mock noise spectra in order to define a robust detection threshold. These simulations assume that the noise is uniform at all frequencies and uncorrelated between pixels. Using 100,000 realizations we find that the probability to have two adjacent pixels with $S/N \geq 3.5$ is less than 0.1 per cent, and therefore this S/N ratio could be used as a detection threshold. To investigate the reliability of these simulations we search for negative peaks, which are expected to be just noise, that satisfy this S/N threshold. We find none, either in the raw or in binned spectra, which supports the adoption of $\xi_{\text{thresh}} = 3.5$ (in two adjacent pixels) as a robust detection threshold.

In order to identify line candidates in our spectra, we search for peaks with $S/N \geq \xi_{\text{thresh}}$, where the noise is estimated as the standard deviation of the whole spectrum. If a peak is identified, we mask a region of 10 pixels centred at the position of the peak (since we know that the full width at half-maximum (FWHM) of lines detected in SMGs can be up to $\sim 1000 \text{ km s}^{-1}$, e.g. Bothwell et al. 2013). This process is repeated until there are no more pixels with $S/N \geq \xi_{\text{thresh}}$. If a line candidate is identified, we inspect it visually to confirm that it does not correspond to a bad baseline. In all our spectra we do not find any such case. In order to find weaker emission lines, we rebin our spectra into 200 km s^{-1} pixels (2 pixels bins) and repeat the process again. Once we have the position of line candidates we carry out a Gaussian line profile fit in order to obtain the central frequency, peak flux, and line width.

Although the general noise is well fitted by a Gaussian distribution (see Fig. 3) and the baseline fluctuations in each spectrum are well confined within the $\pm 2\sigma$ noise range (see Fig. 2), there are some baseline residuals that exceed this range or where the noise seems correlated. These baseline features are usually broad ($> 1000 \text{ km s}^{-1}$) and therefore could preclude the detection of low signal-to-noise ratio ($S/N \lesssim 5$) broad lines (albeit the fraction of SMGs with very broad lines, $> 1000 \text{ km s}^{-1}$, have been found to be low, e.g. 1/32, Bothwell et al. 2013). Broad lines could be missed since our method is based on the detection of high S/N pixels. However, a different method has been developed, which exploits the full spectral information present in the RSR data by cross-correlating the observed spectrum with a theoretical or an empiri-

Table 3. Observational parameters of the lines detected in the RSR spectra, using a blind search. The three blended sources in the HLS J204314.2–214439 target are identified with the extensions /S1, /S2, and /S3. Column 1: name of the source; column 2 and 3: signal-to-noise ratio; column 4: central frequency; column 5: identified transition; column 6: redshift; column 7: integrated flux; column 8: FWHM of the line; column 9: notes.

Source	S/N ^a	S/N ^b	ν_{obs} (GHz)	Transition	z	$S_{\text{CO}}\Delta V$ (Jy km s ⁻¹)	FWHM (km s ⁻¹)	Notes
HLS J045518.0+070103	4.5	7.3	88.051	¹² CO(3–2)	2.927 ^c	4.7 ± 0.8	480 ± 70	Alternative solution $z = 1.618$
HLS J173140.8+225040	4.1	5.7	93.163	¹² CO(3–2)	2.712	2.3 ± 0.8	420 ± 120	z confirmed by IRAM
HLS J204314.2–214439/S1	10.3	15.5	75.827	¹² CO(2–1)	2.040	6.1 ± 0.9	530 ± 60	z confirmed by IRAM and VLT
HLS J204314.2–214439/S2	2.1 ^d	2.0 ^d	81.328	¹² CO(3–2)	3.252	0.5 ± 0.3	260 ± 130	z confirmed by VLT
	5.1	5.7	108.428	¹² CO(4–3)	3.252	1.3 ± 0.4	190 ± 40	
HLS J204314.2–214439/S3	7.7	12.3	81.178	¹² CO(4–3)	4.680	4.8 ± 0.6	570 ± 60	z confirmed by SMA
	5.1	8.0	101.459	¹² CO(5–4)	4.681	2.8 ± 0.5	410 ± 50	

^aThe maximum S/N of the peak pixel from either the raw or the 200 km s⁻¹ binned spectra. In this case, the noise has been estimated as the standard deviation of the whole spectrum after removing the identified lines. ^bThe S/N of the integrated line in the raw spectra (100 km s⁻¹ pixels). ^cTentative solution. ^dThis line is not formally detected by our algorithm, but searched for after the VLT redshift solution was proposed.

cal spectral template (see Yun et al. 2007). A detailed description of this method and its application to the SMG COSMOS AzTEC-1 is described by Yun et al. (2015), and we briefly summarize it here. A cross-correlation product is derived as a function of redshift from the observed spectrum and a model spectral template. This model is weighted by a function which represents the relative strength of different molecular transitions, and for this, an empirical composite spectrum based on observed relative line strengths for high redshift sources (e.g., Spilker et al. 2014) is adopted. This is a powerful method to derive redshifts which takes into account the information of many transitions which are not individually detected with a good S/N. We find that the redshift results are robust, and both methods give consistent results, when the integrated S/N of the lines are sufficiently high (S/N > 5).

In Table 3 we summarize the lines detected in our spectra and Fig. 4 shows them individually. All these detections have at least one peak pixel at S/N ≥ 4.0 in the raw or in the binned spectra and at least one adjacent pixel with S/N ≥ 3.5 (except for a line that is not formally detected by our algorithm, see §3.1.4). However, a better estimation of the reliability of these detections is the S/N of the whole integrated line, which is also reported in Table 3. All the lines detected originally by our algorithm have integrated S/N > 5.

In order to derive the spectroscopic redshifts we have first to associate the detected lines candidates with the correct molecular transitions. The simultaneous frequency coverage of the RSR means at least one CO transition falls within the spectral coverage at all redshifts except for a narrow redshift range (the ‘redshift desert’) in the range $0.58 < z < 1.08$. Furthermore, two or more molecular line transitions fall within the RSR spectral range at $z > 3.15$ if we consider the possibility of a [CI] line detection in addition to the CO lines. On the other hand, since we know that the spectral line energy distribution (SLED) peaks at $J_{\text{up}} = 6 - 5$ for typical SMGs (Bothwell et al. 2013; Spilker et al. 2014), the absence of lines could be used to discard the high-redshift solutions for which we expect more than one line in our spectra. Moreover, our selection of bright sources through galaxy clusters, implies that these very bright SMGs are expected to be gravitationally lensed. This selection tends to exclude low-redshift solutions, $z \lesssim 1 - 1.5$, due to the low probability of being lensed at these redshifts, as discussed by Weiß et al. (2013). Taking these considerations into account, we associate our line candidates with different ¹²CO ($J_{\text{up}} = 2 - 5$) transitions and derive the spectroscopic

redshift for each galaxy (see Table 3). Below we describe briefly the analysis for individual targets.

3.1.1 HLS J045518.0+070103

A line with an integrated S/N=7.3 with a well-fitted Gaussian profile (see Fig. 4) has been detected in this spectrum. The detection of just one line at $\nu = 88.051$ GHz gives a tentative redshift for this galaxy and therefore we have to associate this line with the most probable transition based on other characteristics of the galaxy. If we associate this detection with CO(4–3) at $z = 4.236$, we expect to detect the CO(5–4) transition at $\nu \sim 110.1$ GHz still within our bandpass. The spectrum, however, does not show any line feature around this frequency and, therefore, this solution is discarded. Other possible solutions are CO(3–2) or CO(2–1), which correspond to redshifts of $z = 2.927$ and $z = 1.618$, respectively. As we expect that the probability for these galaxies to lie around $z = 2 - 3$ is higher (e.g. Chapman et al. 2005; Yun et al. 2012; Simpson et al. 2014; Zavala et al. 2014), we have associated our line candidate with the CO(3–2) at $z = 2.927$, although we cannot rule out the alternative lower redshift solution.

3.1.2 HLS J102225.9+500536

For this source we have no detections at S/N ≥ 3.5, either in the raw or in the binned spectrum. One possible explanation is that the galaxy lies in the ‘redshift desert’ of the RSR. However, as we can see in Table 2, this galaxy has the lowest flux density at 1.1 mm, which is less than half of those of the rest of the sample. This would suggest that we need to integrate more in this fainter galaxy to detect a CO emission line. Furthermore the ratio $S_{850\mu\text{m}}/S_{1.1\text{mm}}$ is the largest of the sample, which could be due to a higher temperature, and make more difficult the detection of molecular lines than in the other sources. The upper limit for a line could be calculated using the equation $I_{\text{CO}} = 3\sigma(\delta\nu\Delta\nu_{\text{FWHM}})^{1/2}$, where σ is the rms noise, $\delta\nu$ the velocity resolution, and $\Delta\nu_{\text{FWHM}}$ the line width (e.g. Greve et al. 2005). We adopted a line width of 500 km s⁻¹ similar to the lines detected in the remaining spectra (see Table 3), and a σ derived from the standard deviation of the whole spectrum. Using this equation the upper limit for a line is 1.2 Jy km s⁻¹.

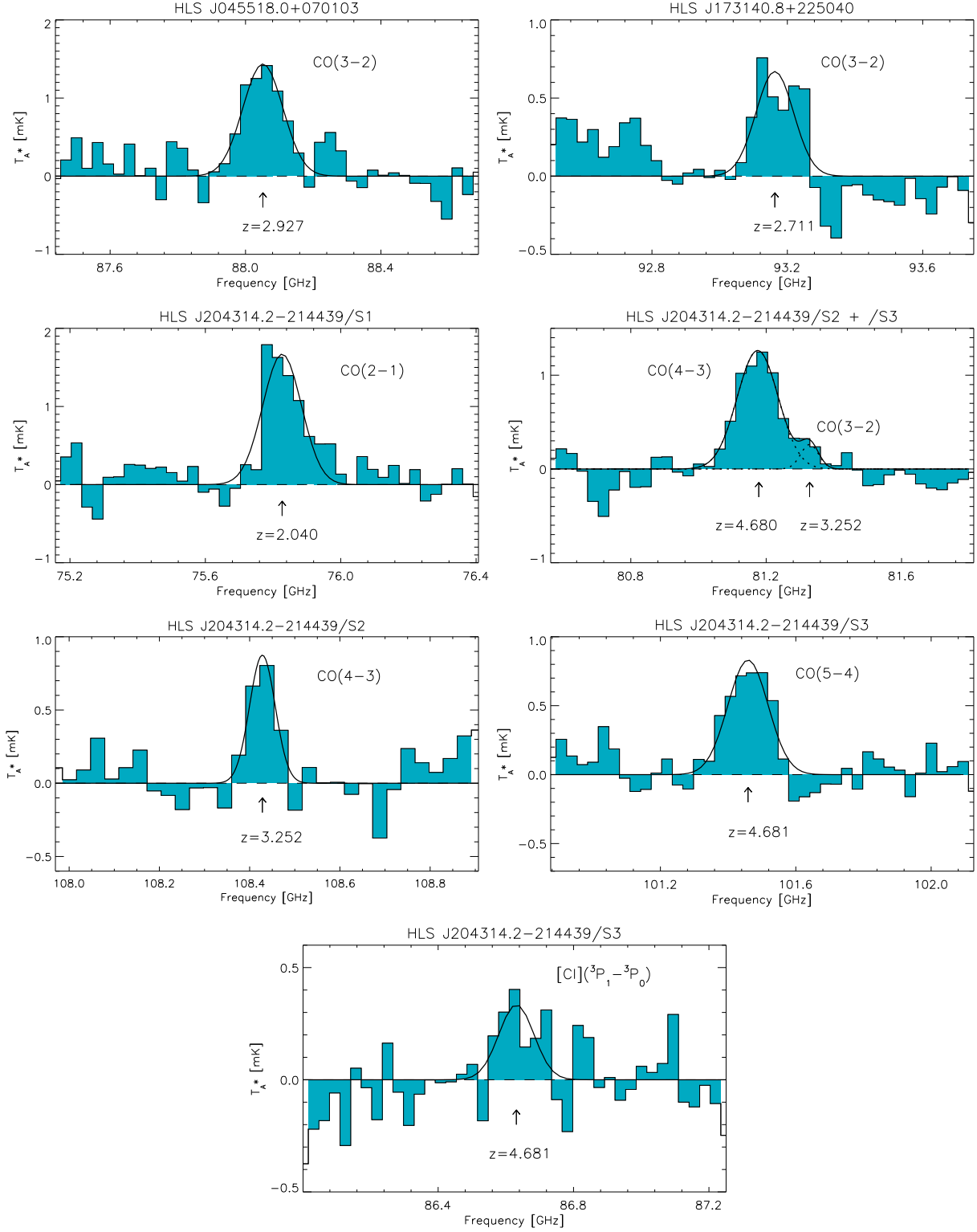


Figure 4. LMT raw spectra at the position of the ^{12}CO and [CI] lines detected in our RSR spectra, best-fitting Gaussian profiles, and redshift derived from each individual line. The three blended sources in the HLS J204314.2–214439 target are identified with the extensions /S1, /S2 and /S3. The [CI]($^3P_1 \rightarrow ^3P_0$) transition at $z = 4.680$ for HLS J204314.2–214439/S3 is only detected at 3σ , and the FWHM of the Gaussian fit is consistent with the line widths of the two ^{12}CO transitions.

3.1.3 *HLS J173140.8+225040*

This is another case of single-line detection at $\nu = 93.163$ GHz with a line integrated $S/N=5.7$. In this case we can associate this transition with CO(4–3) at $z = 3.949$ or CO(3–2) at $z = 2.712$ having rejected the CO(2–1) solution at $z = 1.475$ due to the low probability of lensing at this lower redshift. Independently, earlier observations made by the HLS team had already identified the redshift of this galaxy through a CO redshift search with the IRAM 30-m/EMIR, yielding $z = 2.712$ through the detections of CO(5–4) and CO(3–2) (Dessauges-Zavadsky et al., in preparation), and hence our single line detection unambiguously corresponds to CO(3–2).

The line-shape shows some departure from a single Gaussian profile. However, due to the low pixel-to-pixel S/N , we cannot be certain of the non-Gaussianity, and hence, we decided to perform a single Gaussian fit. If we were to fit two Gaussian profiles, the resulting FWHM for both components are ~ 220 km s $^{-1}$ centred at 93.130 and 93.223 GHz, with a total flux line similar to the one recovered with the one fit procedure.

3.1.4 *HLS J204314.2–214439*

In this case, we have detected four lines with $S/N \geq 3.5$ in the spectrum at $\nu = 75.827, 81.178, 101.459$, and 108.428 GHz. They are not compatible with a single redshift solution, which indicates that we have at least two sources inside our RSR beam.

As a first step to associate these detections with CO transitions, we find that the 81.2 and 101.5 GHz lines agree very well with CO(4–3) and CO(5–4) at $z = 4.680$, however there is no explanation for the 76 and 108 GHz lines at this redshift. The $z = 4.680$ solution has been confirmed after we reanalysed SMA observations, where we found the [CII] transition at $\nu = 334.648$ GHz (see Fig. 5).

The Gaussian fitting to the spectral line gives a FWHM of 432 ± 68 km s $^{-1}$, which is in good agreement with the line widths of the CO emission lines (see Table 3), and a redshift of $z = 4.679$ is also in agreement with our redshift derived from the CO detections. The integrated flux of the line is 19.1 ± 3.6 Jy km s $^{-1}$. This source (hereafter HLS J204314.2–214439/S3) is the highest redshift galaxy detected by the LMT at this time.

Considering next the 75.827 GHz detection, we reject the association with CO(3–2) at $z = 3.56$ since the CO(4–3) line should appear at 101.106 GHz. The closest detected line however is at 101.461 GHz, more than 1000 km/s away, and furthermore we know that this line corresponds to the CO(5–4) transition at $z = 4.680$. Hence we discard this $z = 3.56$ redshift solution. Other evidence that the 76 GHz line arises from a different source is the brightness of the line and the asymmetric line shape seen in Figs 2 and 4, whilst the 81 and 101 GHz lines are more similar in line width and shape. We therefore identify the 76 GHz line as CO(2–1) at $z = 2.040$ (hereafter HLS J204314.2–214439/S1). Moreover, the HLS team independently obtained the same redshift through the detection of CO(4–3) and CO(3–2) with IRAM30m/EMIR (Walth et al., in preparation) and H α with Very Large Telescope (VLT)/Spectrograph for Integral Field Observations in the Near Infrared (SINFONI, Nakajima et al., in preparation).

The remaining 108.428 GHz line does not seem to correspond to any transition at the redshifts of the above galaxies. By inspecting the available VLT/SINFONI data of RXCJ2043, Nakajima et al. (in preparation) found, serendipitously, a strong [OIII] emitter

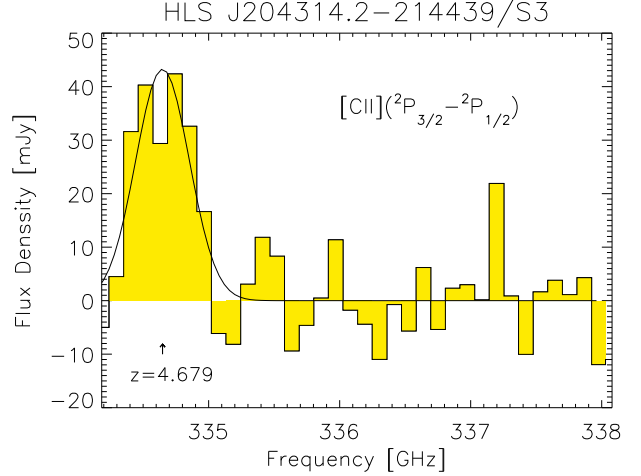


Figure 5. [CII] detection of HLS J204314.2–214439/S3 using SMA observations. The redshift derived from this transition, $z = 4.679$, is in good agreement with the redshift derived from the CO LMT-detected lines. This spectrum has been obtained after combining the signal from the three lensed images of this galaxy. The FWHM and the redshift derived from this detection is in good agreement with the values derived from the CO emission lines detected with the LMT.

falling within the SCUBA-2, AzTEC, and RSR beams. The simultaneous detection of the [OIII] doublet ($\lambda = 4959/5007$ Å) and the H β line confirms an optical redshift of $z = 3.25$. This redshift is consistent with our 108.4 GHz line if we assume it is due to the CO(4–3) transition. At this redshift, we should expect to also detect CO(3–2) at ~ 81.3 GHz, but this is very close to our previously identified line CO(4–3) at $z = 4.68$ (HLS J204314.2–214439/S3). In order to test whether there is any evidence of CO(3–2) at $z \approx 3.25$, we attempt a double Gaussian fit with free central frequencies, widths and amplitudes. The best-fitting Gaussian profiles allowed us to recover the CO(3–2) transition at a redshift consistent with that as predicted by the CO(4–3) transition at $z = 3.252$ and with a similar FWHM (see Fig. 4 and Table 3). We conclude that these two CO lines are most likely associated with a third galaxy at $z = 3.252$ (hereafter HLS J204314.2–214439/S2). In order to estimate the errors for the fits to the CO(3–2) transition we implement a bootstrapping method on the noise and repeat the Gaussian fit 1000 times. The mean and standard deviation of the fits are reported in Table 3.

The detections of three components at widely different redshifts ($z = 2.04, 3.25$, and 4.68) for this blended source confirms the results of theoretical works that predict that some of the blended galaxies are physically unassociated with typical redshift separations $\Delta z \sim 0.9 - 1.5$ (Hayward et al. 2013; Cowley et al. 2015; Muñoz Arancibia et al. 2015).

3.1.5 *Fainter emission lines*

Because of the wide bandwidth of the RSR we can search for additional weaker line transitions of different species that we know to fall within our bandpass, given the redshifts of the galaxies, but which are below the higher detection threshold for blind searches. In this way, for HLS J204314.2–214439/S3 the atomic carbon [CI] ($^3P_1 \rightarrow ^3P_0$) transition at $z = 4.680$ is expected at 86.6 GHz, inside the RSR spectral coverage, where we indeed have evidence for a detection with an integrated line $S/N \approx 3$ (see Fig. 4). This line

has a line width of $\sim 420 \text{ km s}^{-1}$, consistent with the line widths of the CO transitions, and an integrated flux of $\sim 0.9 \pm 0.4 \text{ Jy km s}^{-1}$. However, since this detection is just at a 3σ level, measurements derived from this line have been handled, formally, as upper limits.

3.2 RSR analysis: gas properties

Having identified the most probable line transitions and redshift of each source, we calculate ^{12}CO luminosities of the galaxies using the standard relation given by Solomon & Vanden Bout (2005):

$$L'_{\text{CO}} = 3.25 \times 10^7 S_{\text{CO}} \Delta V \nu_{\text{obs}}^{-2} D_L^2 (1+z)^{-3}, \quad (1)$$

where L'_{CO} is the line luminosity in $\text{K km s}^{-1} \text{ pc}^2$, $S_{\text{CO}} \Delta V$ is the velocity-integrated line flux in Jy km s^{-1} , ν_{obs} is the observed central frequency of the line in GHz, and D_L is the luminosity distance in Mpc. We estimate $S_{\text{CO}} \Delta V$ as the integral of the Gaussian fits to the lines, using Monte Carlo simulations that take into account the errors in the Gaussian parameters (i.e. peak flux density and line width) to estimate the errors.

We continue with an estimation of the H_2 mass from the measured L'_{CO} which requires two steps. First, luminosities originating from higher transitions ($J_{\text{up}} \geq 2$) must be transformed to an equivalent $^{12}\text{CO}(1-0)$ luminosity using a brightness ratio based on an excitation model. Second, once the $L'_{\text{CO}(1-0)}$ has been estimated, the H_2 mass can be derived by the following relationship:

$$M(\text{H}_2) = \alpha L'_{\text{CO}(1-0)}, \quad (2)$$

where α is a conversion factor in units of $M_{\odot} (\text{K km s}^{-1} \text{ pc}^2)^{-1}$.

To transform our $L'_{\text{CO}(J_{\text{up}} \geq 2)}$ to $L'_{\text{CO}(1-0)}$ we have used the brightness ratios reported by Carilli & Walter (2013) for SMGs based on all available literature at the time, and a value of $\alpha = 0.8 M_{\odot} (\text{K km s}^{-1} \text{ pc}^2)^{-1}$ (Downes & Solomon 1998) for the mass transformation. As discussed by Serjeant (2012), differential magnification could affect the line ratios of the CO ladder, however, in cluster lensing it is rare to find strong gradients in the magnification on subarcsecond-scales and therefore the line ratios are usually unaffected (e.g. Danielson et al. 2011). Furthermore, the higher-J CO emission has been shown to be more compact than that of lower-J transitions (e.g. Ivison et al. 2011), which decreases even further the probability of differential magnification.

The resulting ^{12}CO luminosities and H_2 masses are reported in Table 4. The mean H_2 mass of the sample is $(2.0 \pm 0.2) \times 10^{11} M_{\odot} / \mu$, where μ is the lens amplification. We caution that these results adopt average brightness ratios to convert to $L'_{\text{CO}(1-0)}$ which introduce extra uncertainties, as well as our adopted value of α which is a factor of ~ 4 lower than the value used in other works (e.g. Tacconi et al. 2010), and could vary with metallicity and gas properties (Narayanan et al. 2012).

We also estimated the luminosity of the 3σ detection of $[\text{CI}](^3P_1 \rightarrow ^3P_0)$ in HLS J204314.2–214439/S3, finding a luminosity of $\mu L'_{\text{CI}(1-0)} = 5.2 \pm 2.6 \times 10^{10} \text{ K km s}^{-1} \text{ pc}^2$. Comparing this value with the ^{12}CO transitions detected for this galaxy, we have line ratios of $L'_{\text{CI}(1-0)} / L'_{\text{CO}(4-3)} = 0.21 \pm 0.11$ and $L'_{\text{CI}(1-0)} / L'_{\text{CO}(5-4)} = 0.56 \pm 0.29$. These values are consistent with other measurements of SMGs and quasars and do not differ significantly from what is found in low-redshift systems, as discussed by Walter et al. (2011) (see also Alaghband-Zadeh et al. 2013; Popping et al. 2014).

As described by Harris et al. (2012), the line luminosity-line width relation, $L'_{\text{CO}(1-0)} = a(\Delta v_{\text{FWHM}})^b$ (see Fig. 6), could be

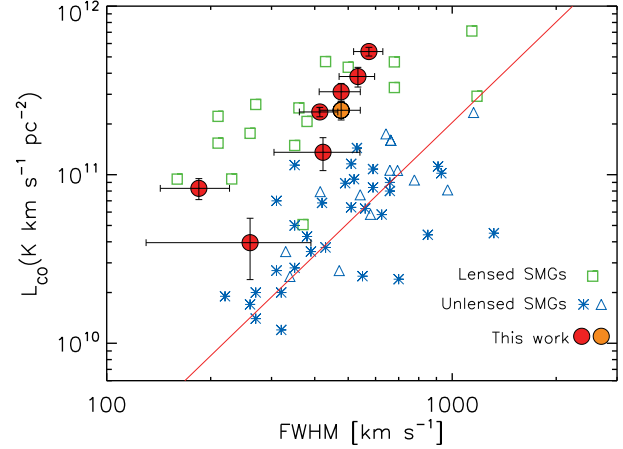


Figure 6. $L'_{\text{CO}(1-0)}$ versus line FWHM for lensed and unlensed SMGs. Red circles represent the measurements from this work and light red is used when we adopt the alternative redshift solution for HLS J045518.0+070103. Estimates derived from each detected transition are plotted individually. Blue triangles are unlensed or lensing-corrected SMGs with CO(1–0) measurements (Carilli et al. 2010; Harris et al. 2010; Ivison et al. 2011; Riechers et al. 2011; Fu et al. 2013) and blue asterisks are SMGs with higher-J CO line measurements converted to CO(1–0) from Bothwell et al. (2013). The red line shows the best-fitting relation for unlensed SMGs $L'_{\text{CO}} = 10^{5.4} \text{FWHM}^2$ derived by Bothwell et al. (2013). The green squares are GBT and VLA CO(1–0) detections of lensed SMGs (Harris et al. 2012; Rawle et al. 2014).

used as an estimator of the lens magnification, μ , if we assume that the magnification only modifies the observed line luminosity (and not the line width). This means that $L'_{\text{apparent}} = \mu L'$ or

$$\mu = \frac{L'_{\text{apparent}}}{L'} = \frac{L'_{\text{apparent}}}{a(\Delta v_{\text{FWHM}})^b}. \quad (3)$$

Our measurements lie within the same region occupied by other lensed SMGs in Fig. 6, which provides circumstantial evidence that amplification due to lensing is present. Table 4 lists the lens magnifications derived from this equation, adopting the line luminosity–line width relation for unlensed SMGs derived by Bothwell et al. (2013) (see also Harris et al. 2012). We measure modest amplification, $\mu \approx 2 - 5$, for the sample.

3.3 SCUBA-2 + AzTEC analysis: dust properties

The dust continuum detections allow us to estimate the dust temperature and IR luminosity once a spectral energy distribution (SED) is fitted to the data. Our determinations of spectroscopic redshifts (see Section 3.1) break the temperature–redshift degeneracy (e.g. Blain et al. 2002), albeit there is still a degeneracy between temperature and spectral index (e.g. Hughes et al. 1993; Casey et al. 2014).

Assuming the dust is isothermal, the dust mass, M_d , is estimated from

$$M_d = \frac{S_\nu D_L^2}{(1+z) \kappa_\nu B(\nu, T_d)}, \quad (4)$$

where S_ν is the flux density at frequency ν , κ_ν is the dust mass absorption coefficient at ν , T_d is the dust temperature, and $B(\nu, T_d)$ is the Planck function at temperature T_d . The dust mass absorption

Table 4. Physical properties derived from the ^{12}CO lines detected in the RSR spectra and the SCUBA-2+AzTEC photometry. Column 1: name of the source; column 2: observed CO luminosity; column 3: CO(1–0) luminosity converted using the factors reported by Carilli & Walter (2013); column 4: H_2 mass assuming $\alpha = 0.8 \text{ M}_\odot (\text{K km s}^{-1} \text{ pc}^2)^{-1}$ (Downes & Solomon 1998); column 5: dust masses estimated from the flux densities at 850 μm and 1.1 mm; column 6: total FIR luminosity; column 7: amplification factor.

Source	$\mu L'_{\text{CO(Jup)}}$ ($\times 10^{10} \text{ K km s}^{-1} \text{ pc}^2$)	$\mu L'_{\text{CO(1-0)}}$ ($\times 10^{10} \text{ K km s}^{-1} \text{ pc}^2$)	$\mu M(\text{H}_2)$ ($\times 10^{10} \text{ M}_\odot$)	μM_d ($\times 10^8 \text{ M}_\odot$)	μL_{FIR} ($\times 10^{12} \text{ L}_\odot$)	μ
HLS J045518.0+070103	20.4 ± 3.6	31.0 ± 5.5	24.8 ± 4.4	25 ± 2.0	63^{+5}_{-7}	~ 4
HLS J173140.8+225040	8.9 ± 3.0	13.5 ± 4.5	10.8 ± 3.6	36 ± 2.0	54^{+5}_{-4}	~ 2
HLS J204314.2–214439/S1	32.4 ± 5.0	38.1 ± 5.8	30.5 ± 4.7	$\sim 15^a$	$\sim 25^a$	~ 5
HLS J204314.2–214439/S2	2.6 ± 1.6	3.9 ± 2.3	3.2 ± 1.9	$\sim 13^a$	$\sim 33^a$	$\sim 3^b$
	3.8 ± 1.2	8.3 ± 2.5	6.7 ± 2.0	$\sim 13^a$	$\sim 33^a$	$\sim 3^b$
HLS J204314.2–214439/S3	24.9 ± 3.2	54.2 ± 6.9	43.3 ± 5.6	$\sim 11^a$	$\sim 44^a$	$\sim 3^b$
	9.3 ± 1.5	23.7 ± 3.9	19.0 ± 3.1	$\sim 11^a$	$\sim 44^a$	$\sim 3^b$

^a The uncertainties in these values are large since the real contribution from each galaxy to the total detected (blended) flux is unknown. We assume equal contribution to the (sub-)mm fluxes by all components. ^b Average of the two transitions.

follows the same power law as the optical depth, $\kappa \propto \nu^\beta$ with a normalization of $\kappa_d(850\mu\text{m}) = 0.15 \text{ m}^2 \text{ kg}^{-1}$ (Dunne et al. 2003).

We fit modified blackbody functions fixed at the derived redshift of each galaxy, to the continuum photometry data in Table 2 along with the SPIRE photometry, in order to estimate the dust temperature. For the HLS J204314.2–214439 blended galaxies we adopt a dust temperature of $T = 37 \pm 8 \text{ K}$ as that measured in lensed galaxies (Weiß et al. 2013; see also Harris et al. 2012) since the contribution from each galaxy to the total blended flux is unknown. This value is consistent with the estimated temperatures of the other galaxies in our sample (e.g. 38 ± 3 and $35 \pm 3 \text{ K}$, for HLS J045518.0+070103 and HLS J173140.8+225040, respectively).

Using this temperatures and a fixed emissivity index of $\beta = 1.7$ (empirical fits to the observed long wavelength SEDs suggest $\beta = 1.5 - 2$; e.g. Dunne & Eales (2001); Chapin et al. 2009; Magnelli et al. 2012), we have derived the dust mass for each galaxy from the flux density at both 850 μm and 1.1 mm, and extrapolating κ to the observed rest-frame for each galaxy. These values are reported in Table 4 and have a mean dust mass of $(2.0 \pm 0.2) \times 10^9 \text{ M}_\odot/\mu$. If we extrapolate the observed spectral index to use $\kappa_d(850\mu\text{m})$ directly, the mean dust mass increases by a factor of ~ 2 . These calculations do not include uncertainties in κ , which could be at least a factor of 3 (Dunne et al. 2003). For HLS J204314.2–214439/S1, HLS J204314.2–214439/S2, and HLS J204314.2–214439/S3 we have assumed they each contribute a third of the total (blended) flux density, as a first approximation. A full multi-wavelength analysis of this triple system, including interferometric observations, will be presented by Walth et al. (in preparation).

Finally, the estimated FIR luminosities (L_{FIR} ; 42.5 – 122.5 μm), which arise from the SED fitting, are reported in Table 4 and discuss below.

4 DISCUSSION

4.1 The $L'_{\text{CO}}\text{--}L_{\text{FIR}}$ relation

The SFE, with which the molecular gas is being turned into stars, can be inferred from our observations. This quantity is often estimated by the ratio $\text{SFR}/M(\text{H}_2)$ – the inverse of the gas depletion time – however, a more straightforward estimate of the SFE is the continuum-to-line luminosity ratio, $L_{\text{FIR}}/L'_{\text{CO(1-0)}}$, because

it does not depend on the CO– H_2 conversion factor, α . This describes, in observational terms, the relationship between the luminosity due to star formation and the gas content.

In Fig. 7 we plot our galaxies with CO detections, after correcting for magnification, on to the $L'_{\text{CO}} - L_{\text{FIR}}$ plane, including observations of local (ultra-) luminous infrared galaxies (U)LIRGs (Sanders et al. 1991; Solomon et al. 1997) and other SMGs (Bothwell et al. 2013). We also show the three power-law fits derived by Bothwell et al. (2013) to the local (U)LIRGs alone (with a slope of 0.79 ± 0.08), the SMGs alone (0.93 ± 0.14), and the combined sample (0.83 ± 0.09). Our results are consistent with other SMG observations, but they are also consistent with the fit to the combined sample and the (U)LIRGs alone. Furthermore, as discussed by Bothwell et al., our analysis requires extrapolating from high- J_{up} ^{12}CO transitions to $^{12}\text{CO(1-0)}$, which introduces extra uncertainties without brightness temperature ratio measurements for individual sources. Although we have used the estimated amplification factors, the ratio between CO and FIR luminosity is independent of magnification, assuming no differential amplification, which is usually the case in the cluster lensing.

4.2 The gas-to-dust ratio

Constraining the molecular gas properties of a large sample of non-gravitationally amplified SMGs with spectroscopic observations requires a significant investment of time at present (Bothwell et al. 2013). An alternative approach to estimate the molecular gas mass is to use the continuum emission of the dust in order to estimate the dust mass, and then use an appropriate gas-to-dust ratio, δ_{GDR} , to derive the total mass of the molecular ISM. However, this gas-to-dust ratio is only well constrained in Milky Way molecular clouds and local galaxies (e.g. Draine et al. 2007), and only in a few SMGs (e.g. Swinbank et al. 2013).

Combining our estimation of H_2 gas mass with the dust mass resulting from the SCUBA-2 and AzTEC flux densities, we estimate the gas-to-dust ratio for these high-redshift galaxies, which is independent of the lensing amplification, assuming that both gas and dust are amplified by the same factor, which should be applicable to these cluster-lensed sources. Using our independent estimation of these quantities we have found a weighted mean gas-to-dust ratio of $\delta_{\text{GDR}} \approx 55$ for the two galaxies without direct evidence of blending (HLS J045518.0+070103 and HLS

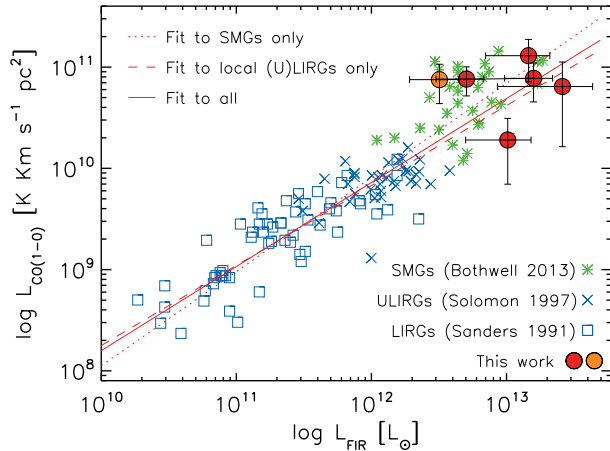


Figure 7. Lens-corrected CO luminosity versus FIR luminosity ($L'_{\text{CO}} - L_{\text{FIR}}$) for our sample, in red circles, and in light red if we adopt the alternative CO solution for HLS J045518.0+070103. For galaxies with more than one detected transition we have plotted the mean L'_{CO} . For comparison, other SMGs are plotted (Bothwell et al. 2013) along with local LIRGs (Sanders et al. 1991) and ULIRGs (Solomon et al. 1997). Best-fitting slopes derived by Bothwell et al. (2013) to SMGs, local (U)LIRGs, and all three combined samples are overplotted. They have slopes of 0.93 ± 0.14 , 0.79 ± 0.08 , and 0.83 ± 0.09 , respectively.

J173140.8+225040). If we also consider the blended galaxies, assuming they all contribute equally to the total integrated flux with intrinsic flux density errors of 50 per cent, we find a weighted mean $\delta_{\text{GDR}} \approx 75$. The scatter in these measurements is however high ($\delta_{\text{GDR}} = 20 - 390$), especially for the blended sources. Our estimated mean values are consistent with those of non lensed SMGs, $\delta_{\text{GDR}} = 90 \pm 25$ (Swinbank et al. 2013), and also with the lensed $z = 6.3$ HFLS3 galaxy, $\delta_{\text{GDR}} \sim 80$ (Riechers et al. 2013). These ratios are smaller than local values, as also discussed in the literature (e.g. Kovács et al. 2006; Santini et al. 2010; Dessauges-Zavadsky et al. 2015), which supports the ‘dust richness’ interpretation of SMGs. For reference, the Milky Way has a gas-to-dust ratio of $\sim 135 - 185$ (Draine et al. 2007), and local LIRGs 120 ± 28 (Wilson et al. 2008). We emphasize, however, that the scatter in our measurements, especially for the blended sources, is high, and some of our estimated individual ratios for the blends overlap with the local values.

5 SUMMARY

We present AzTEC 1.1 mm continuum observations and RSR spectra taken with the LMT, as part of the LMT Early Science campaign, of a sample of four cluster-lensed SMGs.

We surprisingly find that one of the four targets studied is a blend of three galaxies at different redshifts. This confirms that the multiplicity that has been found by high-resolution interferometric observations in normal SMGs (Wang et al. 2011; Smolčić et al. 2012; Hodge et al. 2013) is also present in lensed galaxies, although our search focuses on spectroscopically distinct components. This also confirms the theoretical predictions of physically unassociated components in blended galaxies (e.g. Hayward et al. 2013; Cowley et al. 2015; Muñoz Arancibia et al. 2015). The sam-

ple, though, is too small to derive firm conclusions on the statistics of spectroscopic multiplicity.

Of the five reported redshifts, just one was obtained with the robust blind detections of two lines within a single RSR spectrum. Three other redshifts were confirmed thanks to the detection of different transitions with other telescopes, and the remaining one is a tentative solution.

The estimated mean H_2 gas mass estimated from the CO lines detected is $(2.0 \pm 0.2) \times 10^{11} M_{\odot}/\mu$ and the mean dust mass estimated from the continuum data is $(2.0 \pm 0.2) \times 10^9 M_{\odot}/\mu$, where μ is the lensing factor. These results are self-consistent using either the 850 μm or 1.1 mm data. Using the line width–luminosity relation for SMGs from Bothwell et al. (2013) we estimate $\mu \sim 2 - 5$.

We infer from our independent estimations of gas and dust masses a weighted mean gas-to-dust ratio $\delta_{\text{GDR}} \approx 55 - 75$, which, given the little likelihood of differential amplification at mid-J transitions, should be independent of the amplification factor. These values are consistent with other measurements of SMGs and lower than the estimated ratios for local galaxies.

Finally, we estimate the FIR luminosity using our photometric data and with this the SFE of our galaxies through the $L'_{\text{CO}} - L_{\text{FIR}}$ relationship. Our bright galaxies follow the correlation found for local (U)LIRGs and other SMGs, with a close to linear slope. This suggests that, at the largest luminosities sampled by our systems, the SFE is maintained arguing for a universal value from the lowest to the highest redshifts and from the smallest to the largest mass reservoirs of molecular gas.

The successful blind redshift search in these bright SMGs, performed during this LMT Early Science operation period with the current 32-m diameter illuminated surface, highlights the competitiveness of this new facility. The sensitivity that will be achieved with the expanded primary surface of the full 50-m diameter LMT will place this telescope among the most powerful facilities to perform spectroscopic CO surveys (see Frayer et al. 2011 for a comparison of different telescopes), allowing us to estimate redshifts for significant samples of highly obscured dusty star-forming galaxies which are not measurable with even the largest optical and near-IR telescopes.

ACKNOWLEDGMENTS

We would like to thank an anonymous referee for a constructive and helpful report.

This work would not have been possible without the longterm financial support from the Mexican Science and Technology Funding Agency, Consejo Nacional de Ciencia y Tecnología (CONACYT) during the construction and early operational phase of the Large Millimeter Telescope *Alfonso Serrano*, as well as support from the US National Science Foundation via the University Radio Observatory program, the Instituto Nacional de Astrofísica, Óptica y Electrónica (INAOE) and the University of Massachusetts (UMASS).

This work has been mainly supported by Mexican CONACyT research grants CB-2011-01-167291 and CB-2009-133260, JAZ is also supported by a CONACyT studentship. JEG acknowledges the Royal Society. IS acknowledges support from STFC (ST/L00075X/1), the ERC Advanced Investigator programme DUSTYGAL (321334) and a Royal Society/Wolfson Merit Award. AMS acknowledges an STFC advanced fellowship through grant ST/H005234/1.

The James Clerk Maxwell Telescope is operated by the Joint

Astronomy Centre on behalf of the Science and Technology Facilities Council of the United Kingdom, the National Research Council of Canada, and (until 2013 March 31) the Netherlands Organisation for Science Research. Additional funds for the construction of SCUBA-2 were provided by the Canada Foundation for Innovation.

The Submillimeter Array is a joint project between the Smithsonian Astrophysical Observatory and the Academia Sinica Institute of Astronomy and Astrophysics and is funded by the Smithsonian Institution and the Academia Sinica.

REFERENCES

- Alaghband-Zadeh S. et al., 2013, *MNRAS*, 435, 1493
- Barger A. J., Cowie L. L., Sanders D. B., Fulton E., Taniguchi Y., Sato Y., Kawara K., Okuda H., 1998, *Nature*, 394, 248
- Blain A. W., Smail I., Ivison R. J., Kneib J.-P., Frayer D. T., 2002, *Phys. Rep.*, 369, 111
- Böhringer H. et al., 2004, *A&A*, 425, 367
- Bothwell M. S. et al., 2013, *MNRAS*, 429, 3047
- Carilli C. L., Walter F., 2013, *ARAA*, 51, 105
- Carilli C. L. et al., 2010, *ApJ*, 714, 1407
- Casey C. M., Narayanan D., Cooray A., 2014, *Phys. Rep.*, 541, 45
- Chapin E. L. et al., 2009, *MNRAS*, 398, 1793
- Chapin E. L., Berry D. S., Gibb A. G., Jenness T., Scott D., Tilanus R. P. J., Economou F., Holland W. S., 2013, *MNRAS*, 430, 2545
- Chapman S. C., Blain A. W., Smail I., Ivison R. J., 2005, *ApJ*, 622, 772
- Cowley W. I., Lacey C. G., Baugh C. M., Cole S., 2015, *MNRAS*, 446, 1784
- Cox P. et al., 2011, *ApJ*, 740, 63
- Danielson A. L. R. et al., 2011, *MNRAS*, 410, 1687
- Dessauges-Zavadsky M. et al., 2015, *A&A*, 577, A50
- Downes D., Solomon P. M., 1998, *ApJ*, 507, 615
- Draine B. T. et al., 2007, *ApJ*, 663, 866
- Dunne L., Eales S. A., 2001, *MNRAS*, 327, 697
- Dunne L., Eales S., Ivison R., Morgan H., Edmunds M., 2003, *Nature*, 424, 285
- Ebeling H., Edge A. C., Böhringer H., Allen S. W., Crawford C. S., Fabian A. C., Voges W., Huchra J. P., 1998, *MNRAS*, 301, 881
- Ebeling H., Edge A. C., Henry J. P., 2001, *ApJ*, 553, 668
- Ebeling H., Edge A. C., Mantz, A., Barret E., Henry J. P., Ma C. J., van Speybroeck L., 2010, *MNRAS*, 407, 83
- Egami E. et al., 2010, *A&A*, 518, L12
- Erickson N., Narayanan G., Goeller R., Grosslein R., 2007, in Baker A. J., Glenn J., Harris A. I., Magnum J. G., Yun M. S., eds, *ASP Conf. Ser. Vol. 375, From Z-Machines to ALMA: (Sub)Millimeter Spectroscopy of Galaxies*, Astron. Soc. Pac., San Francisco, p.71
- Fixsen D. J., Dwek E., Mather J. C., Bennett C. L., Shafer R. A., 1998, *ApJ*, 508, 123
- Frayer D. T. et al., 2011, *ApJ*, 726, L22
- Fu H. et al., 2013, *Nature*, 498, 338
- Geach J. E. et al., 2013, *MNRAS*, 432, 53
- Greve T. R. et al., 2005, *MNRAS*, 359, 1165
- Harris A. I., Baker A. J., Zonak S. G., Sharon C. E., Genzel R., Rauch K., Watts G., Creager R., 2010, *ApJ*, 723, 1139
- Harris A. I. et al., 2012, *ApJ*, 752, 152
- Hayward C. C., Behroozi P. S., Somerville R. S., Primack J. R., Moreno J., Wechsler R. H., 2013, *MNRAS*, 434, 2572
- Hodge J. A. et al., 2013, *ApJ*, 768, 91
- Holland W. S. et al., 2013, *MNRAS*, 430, 2513
- Hughes D. H., Robson E. I., Dunlop J. S., Gear W. K., 1993, *MNRAS*, 263, 607
- Hughes D. H. et al., 1998, *Nature*, 394, 241
- Hughes D. H., et al., 2010, *Proc. SPIE*, 7733, 7733 12
- Huynh M. T. et al., 2014, *MNRAS*, 443, L54
- Ivison R. J. et al., 2002, *MNRAS*, 337, 1
- Ivison R. J. et al., 2007, *MNRAS*, 380, 199
- Ivison R. J., Smail I., Papadopoulos P. P., Wold I., Richard J., Swinbank A. M., Kneib J.-P., Owen F. N., 2010, *MNRAS*, 404, 198
- Ivison R. J., Papadopoulos P. P., Smail I., Greve T. R., Thomson A. P., Xilouris E. M., Chapman S. C., 2011, *MNRAS*, 412, 1913
- Knudsen K. K., Neri R., Kneib J.-P., van der Wer, P. P., 2009, *A&A*, 496, 45
- Kovács A., Chapman S. C., Dowell C. D., Blain A. W., Ivison R. J., Smail I., Phillips T. G., 2006, *ApJ*, 650, 592
- Magnelli B. et al., 2012, *A&A*, 539, AA155
- Mann A. W., Ebeling H., 2012, *MNRAS*, 420, 2120
- Muñoz Arancibia A. M., Navarrete F. P., Padilla N. D., Cora S. A., Gawiser E., Kurczynski P., Ruiz A. N., 2015, *MNRAS*, 446, 2291
- Narayanan D., Krumholz M. R., Ostriker E. C., Hernquist L., 2012, *MNRAS*, 421, 3127
- Planck Collaboration XVI, 2014, *A&A*, 571, A16
- Pope A. et al., 2008, *ApJ*, 675, 1171
- Popping G., Pérez-Beaupuits J. P., Spaans M., Trager S. C., Somerville R. S., 2014, *MNRAS*, 444, 1301
- Puget J.-L., Abergel A., Bernard J.-P., Boulanger F., Burton W. B., Desert F.-X., Hartmann D., 1996, *A&A*, 308, L5
- Rawle T. D. et al., 2014, *ApJ*, 783, 59
- Riechers D. A., Hodge J., Walter F., Carilli C. L., Bertoldi F., 2011, *ApJL*, 739, L31
- Riechers D. A. et al., 2013, *Nature*, 496, 329
- Sanders D. B., Scoville N. Z., Soifer B. T., 1991, *ApJ*, 370, 158
- Santini P. et al., 2010, *A&A*, 518, L154
- Santini P. et al., 2014, *A&A*, 562, A30
- Scott K. S. et al., 2008, *MNRAS*, 385, 2225
- Serjeant S., 2012, *MNRAS*, 424, 2429
- Simpson J. M. et al., 2014, *ApJ*, 788, 125
- Simpson J. M., Swinbank et al., 2015, *ApJ*, accepted
- Smail I., Ivison R. J., Blain A. W., 1997, *ApJ*, 490, L5
- Smolčić V. et al., 2012, *A&A*, 548, AA4
- Soifer B. T., Neugebauer G., Houck J. R., 1987, *ARA&A*, 25, 187
- Solomon P. M., Downes D., Radford S. J. E., & Barrett J. W., 1997, *ApJ*, 478, 144
- Solomon P. M., Vanden Bout P. A., 2005, *ARA&A*, 43, 677
- Spilker J. S. et al., 2014, *ApJ*, 785, 149
- Swinbank A. M. et al., 2010, *Nature*, 464, 733
- Swinbank M. et al., 2014, *MNRAS*, 438, 1267
- Tacconi L. J. et al., 2010, *Nature*, 463, 781
- Walter F., Weiß, A., Downes, D., Decarli R., & Henkel C., 2011, *ApJ*, 730, 18
- Wang W.-H., Cowie L. L., Barger A. J., Williams J. P., 2011, *ApJ*, 726, L18
- Weiß A. et al., 2013, *ApJ*, 767, 88
- Wilson C. D. et al., 2008, *ApJS*, 178, 189
- Wilson G. W. et al., 2008, *MNRAS*, 386, 807
- Yun M. S., Heyer M., Arctaxaga I., 2007, in Baker A. J., Glenn J., Harris A. I., Magnum J. G., Yun M. S., eds, *ASP Conf. Ser.*

Vol. 375, From Z-Machines to ALMA: (Sub)Millimeter Spectroscopy of Galaxies, Astron. Soc. Pac., San Francisco, p. 174

Yun M. S. et al., 2012, MNRAS, 420, 957

Yun M. S., Aretxaga I., Gurwell M. A., et al., 2015, MNRAS, submitted

Zavala J. A., Aretxaga I., Hughes D. H., 2014, MNRAS, 443, 2384

This paper has been typeset from a \TeX / \LaTeX file prepared by the author.